11th International Symposium on Turbulence and Shear Flow Phenomena (TSFP11)
Southampton, UK, July 30 to August 2, 2019

INTERACTION OF A TURBULENT BOUNDARY LAYER WITH A BIO-INSPIRED FLEXIBLE CANOPY

Nikolaos Beratlis
School for Eng. Matter, Transport and Energy
Arizona State University
Tempe, AZ 85281
nikos.beratlis@gmail.com

Elias Balaras
Department of Mech. & Aerospace Eng.
The George Washington University
Washington, DC 20052
balaras@gwu.edu

Kyle Squires
School for Eng. of Matter, Transport and Energy
Arizona State University
Tempe, AZ 85281
squires@asu.edu

INTRODUCTION

Interaction of a turbulent boundary layer with a flexible canopy is a common problem encountered in diverse applications ranging from sports ball aerodynamics to atmospheric flows. In felt covered tennis balls, for example, the felt filaments experience pressure drag that contributes up to 40% of the total drag (see Mehta & Pallis (2004)). As the free-stream velocity is increased, many of the filaments that are initially standing almost perpendicular to the surface are forced to lay down due to aerodynamic drag effects and the contribution of the *fuzz* drag is reduced. Another characteristic example, which has been the main inspiration for the present work, is the flexible canopy formed by the feathers on an owl wing. It is hypothesized that the structure of such canopies contributes to their ability to fly almost silently. Geyer *et al.* (2013) measured the noise generated by different species of birds as the fly over an array of microphones and found that owl flight produces aerodynamic noise that is indeed a few decibels below that of other birds, even if flying at the same speed. This noise reduction is significant at frequencies above 1.6 kHz, while at frequencies above 6.3 kHz noise levels are too low to be measured. Geyer *et al.* (2013) also performed experiments in an aeroacoustic wind tunnel using prepared wings from different birds. Their findings further confirmed that the silent owl flight is a consequence of the special wing and plumage adaptations of the owls and not a consequence of their lower flight speed only.

Klan *et al.* (2012) and Winzen *et al.* (2013) conducted wind tunnel experiments on a model wing based on the geometry of the wing of a barn owl in an attempt to investigate the impact of artificial surface filaments on the overall flow field. The wind was either smooth or covered with different types of velvet-like surface that approximated the feather canopy of the barn-owl wing. The Reynolds number based on the wind cord length varied from 20,000 to 60,000 and the angle of attack varied from 0° to 6°. They used PIV to measure the flow field around the wing. They found that the geometry of the owl wing causes the flow to separate on the top part giving rise to a recirculation bubble. The free shear layer that forms above the recirculation bubble becomes unstable and as a result when the flow reattaches the boundary layer is turbulent. In wings with velvet surfaces the separation bubble is either reduced or stabilized, i.e., it does not change depending on the angle of attack, when a velvet canopy is present. In some cases, the separation bubble was fully eliminated due to an earlier laminar-to-turbulent transition. Differences were also observed downstream of the separation bubble where the flow is turbulent. In particular, the space-time correlation of the wall-normal velocity fluctuations showed that the decay of the vortical structures is influenced by the velvet structures. When flexible filaments are present the convection velocity of the eddies is reduced.

A detailed examination of the structure of the down canopy has been performed by Clark *et al.* (2014). Using feathers from four different species of owls and microscope imaging techniques they showed that the down canopy is organized into layers. The lowest layer or substrate is formed by a thick mat of fibers. The fibers grow nearly perpendicular but then lean over to form a canopy suspended 0.5mm above the substrate. The average length of the fibers is between 1-2mm and the open area ratio of the canopy is approximately 70%. The Reynolds number based on the length of the fiber is 100, while that based on the diameter of the fiber can be as low as 7.

While experiments and simulations of a turbulent boundary layer interacting with flexible filaments have been performed, the work has focused on drag reduction (see Brucker, 2011; Sundin & Bagheri, 2019) and wake manipulation behind bluff bodies (see Pinelli *et al.*, 2017). A commonly adopted computational approach starts from the micro-structure and extracts microscopic physical properties, such as permeability, effective elasticity etc, which are then introduced in a macroscopic model. The procedure is called upscaling and typically starts from a representative elementary volume (REV) and generate an equivalent continuous homogenized model. A widely used approach is the volume averaging method (VANS) by Whitaker (1993). It averages the Navier-Stokes equations over an elementary cell representative of the porous structure the size of the

REV, where periodicity is assumed for all flow variables. Although the method has been developed for rigid media it has also be extended to poroelastic media with the introduction of closure relations for the motion of the structure (see Le Bars & Worster, 2006). Another strategy is described by Mei & Vernescu (2010) and consists in implementing a homogenization technique based on a multiscale analysis. The starting point is the same as the volume averaging method and a proper expansion of the unknown fields in terms of powers of a small parameter is assumed. Assuming the convective terms are sufficiently small the resulting equations at leading order are self-contained. If this assumption is not valid then there is the need to introduce a closure relation. All the above techniques refer to the solution of the flow deeply inside a porous medium, far from the boundaries. The problem of the interface conditions between the pure fluid and the homogenized porous region is critical for the overall accuracy, and today the proper way to address it is still open for debate.

High-fidelity computations reproducing closely the geometry of the solid skeleton, where the pore-scale flow is directly resolved together with the outer flow does not suffer from the above limitations but are computationally expensive. Kuwata & Suga (2017) for example, used direct numerical simulations (DNS) of turbulent channel flow over a porous layer, where the directional permeabilities were modulated by assembling arrays of hollows cubes along the Cartesian directions. To reduce the cost typically the filaments are treated as infinitesimally thin bodies and the force exerted by the structure on the fluid is then spread onto the Eulerian grid points near the boundary (see Tian *et al.*, 2011; Pinelli *et al.*, 2017). As a result the flow across the flexible body is not fully resolved. In the present work we will report DNS of turbulent flow interacting with a flexible canopy and examine its impact on the flow statistics. Unlike previous work the flow around the flexible filaments is resolved by employing a very fine grid. The details on the methodologies and results are given below.

METHODOLOGIES

We will consider the case of a fully developed turbulent channel flow, where one of the walls is covered by a flexible canopy consisting of an array of filaments randomly distributed to match the desired open area ratio. The coordinates x,y, and z represent the streamwise, wall normal and spanwise directions respectively. The incompressible fluid flow is governed by the Navier-Stokes equations:

$$\frac{\partial \mathbf{u}}{\partial t} + \mathbf{u}\cdot\nabla\mathbf{u} = -\nabla p + \frac{1}{Re}\nabla^2\mathbf{u}, \qquad (1)$$

where $\mathbf{u}$ is the velocity vector, p is the pressure, and Re is the Reynolds number based on the kinematic viscosity of the fluid, the mean bulk velocity U_b and the channel half height h. The dynamic deformations of the filaments are governed by an inextensible Kirchhoff rod model (see for example Huang *et al.*, 2007). The Kirchhoff rod model is well suited to model such structures, because it enables control of the undeformed shape and flexibility among other parameters to match the characteristics of the bio-inspired canopies considered in the present study. The governing equation for a flexible inextensible filament are written in Lagrangian non-dimensional form as:

$$\begin{aligned}\frac{\partial^2 \mathbf{X}}{\partial t^2} =& \frac{\partial}{\partial s}\left(T\frac{\partial \mathbf{X}}{\partial s}\right) - \frac{\partial^2}{\partial s^2}\left(\gamma\frac{\partial^2(\mathbf{X}-\mathbf{X_i})}{\partial s^2}\right)\\ &+Fr\frac{\mathbf{g}}{g} - \alpha\cdot\mathbf{F} + \mathbf{F_r}\end{aligned} \qquad (2)$$

where s is the arclength, going from 0 at the bottom of the filament to L at the tip, $\mathbf{X} = (X(s,t), Y(s,t), Z(s,t))$ is the position, T is the tension force along the filament axis, $\mathbf{F}$ is the fluid force exerted on the filament, and $\mathbf{F_r}$ denotes the repulsive forces between nearby filaments. In Eq. 2, $\alpha = \rho/\rho_s$ denotes the ratio of the density of fluid to that of the filament. The second term on the right hand side of Eq. 2 represents the bending force and $\mathbf{X_i}$ denoted the undeformed state of the filament. The constant γ is a dimensionless parameter defined as $\Gamma/\rho_s U^2 L^2$, where Γ and ρ_s are the bending rigidity and densityof the filaments. It represents the ratio of the bending to inertial forces. The inextensibility condition is expressed by:

$$\frac{\partial \mathbf{X}}{\partial s}\cdot\frac{\partial \mathbf{X}}{\partial s} = 0 \qquad (3)$$

The tension force, T, in Eq. 2 is determined by the constraint of inextensibility by solving the following Poisson equation:

$$\begin{aligned}\frac{\partial \mathbf{X}}{\partial s}\cdot\frac{\partial^2}{\partial s^2}\left(T\frac{\mathbf{X}}{\partial s}\right) =& \frac{1}{2}\frac{\partial^2}{\partial t^2}\left(\frac{\partial \mathbf{X}}{\partial s}\cdot\frac{\partial \mathbf{X}}{\partial s}\right) - \frac{\partial^2 \mathbf{X}}{\partial t\partial s}\cdot\frac{\partial^2 \mathbf{X}}{\partial t\partial s}\\ &-\frac{\partial \mathbf{X}}{\partial s}\cdot\frac{\partial}{\partial s}\left(\gamma\frac{\partial^2(\mathbf{X}-\mathbf{X_i})}{\partial s^2} - \mathbf{F} + \mathbf{F_r}\right)\end{aligned} \qquad (4)$$

At the free end ($s = L$) the boundary conditions for the filaments are $T = 0$, $\partial^2\mathbf{X}/\partial s^2 = (0,0,0)$ and $\partial^3\mathbf{X}/\partial s^3 = (0,0,0)$. At the bottom wall the filaments are clamped and the boundary conditions are $\partial T/\partial s = 0$, $\mathbf{X} = \mathbf{X_{wall}}$ and $\partial\mathbf{X}/\partial s = (0,1,0)$.

A staggered grid is used in the Lagrangian coordinate system, with the tension defined on the interfaces and the other variables defined on the nodes. All spatial derivatives are approximated using second order central differences. For the time advancement of the kinematics all terms except the bending and repulsive forces are treated implicitly.

To validate the Kirchhoff rod model we performed simulations of a hanging filament without ambient fluid under a gravitational force. The filament is initially held stationary at an angle θ_0 from the vertical and released at $t = 0$. The initial position of the filament is given by $X(s,t=0) = L\cdot cos(\theta_0)$ and $Y(s,t=0) = L\cdot sin(\theta_0)$, where x is the direction of the gravity. At the hanging end a simply supported boundary condition is used, namely $\partial T/\partial s = 0$, $\mathbf{X} = \mathbf{X_{wall}}$ and $\partial\mathbf{X}^2/\partial s^2 = (0,0,0)$. The motion of the filament with ($\gamma = 0.1$) and without ($\gamma = 0$) bending force at various time steps is shown in Fig. 1. The motion is from left to right. In the simulations $L = 1$, $Fr = 10$ and $\theta_0 = 0.1\pi$. In the absence of a bending force the filament is very flexible and the free end rolls up towards the right at the end of the rightwards motion. When $\gamma = 0.1$ the filament maintains its predeformed shape throughout the motion and the roll-up is inhibited. The motion in this case resembles more that of a pendulum.

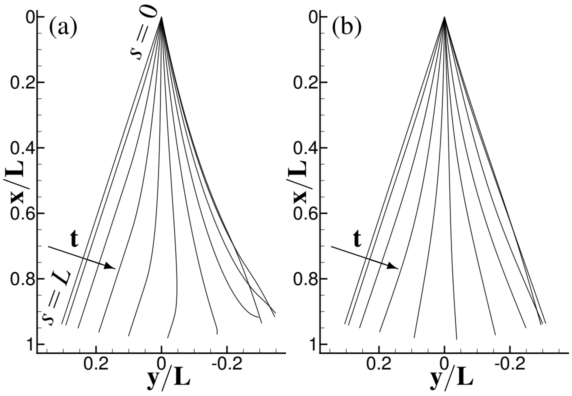

Figure 1. Motion of a hanging filament at various time instants starting at $t = 0$ and separated by $\Delta t = 0.3$. The motion is from left to right. a) $\gamma = 0$ (no bending force) and b) $\gamma = 0.1$.

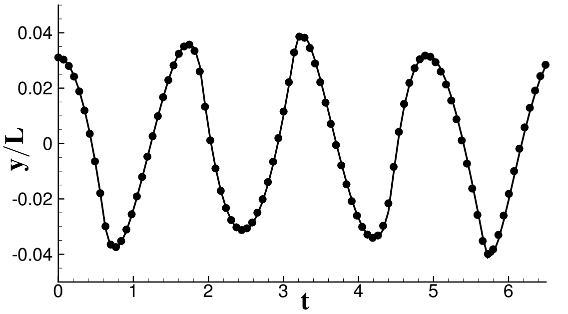

Figure 2. Time history of the free end of a hanging filament with $\gamma = 0$ and $\theta_0 = 0.01\pi$. Lines represent: • numerical solution, - analytical solution.

An analytical solution for the motion of the filament exists when the swing amplitude is small and the bending force is neglected (see Huang *et al.*, 2007). A comparison of the analytical solution with the simulation ($\gamma = 0$, $\theta_0 = 0.01\pi$) is shown in Fig. 2, where the free end position of the filament is plotted. The agreement is excellent.

The complex fluid structure interaction problem is solved using the immersed boundary formulation discussed in Balaras (2004); Yang & Balaras (2006). The equations governing the fluid flow are discretized on a structured Cartesian grid. Each filament is represented by a set of equally spaced marker points. To account for its finite thickness a cylindrical aerodynamic shell is defined to give it the desired three-dimensional shape (see Fig. 3). Forces from the fluid side are computed on the aerodynamic shell, and then transferred to the Kirchhoff rod model to compute the structural deformations. Due to the proximity of the filaments to one another a collision model was used to account for their short-range interaction. We use the collision model proposed in Wan & Turek (2007) for simulations with spherical particles, where a tuned short range repulsive force is defined to avoid overlapping. At each timestep the distance between the closest filament core markers is calculated and a repulsive force is computed as follows:

$$\mathbf{F_r} = \begin{cases} 0 & d > 2.5 \cdot r \\ \frac{\delta \mathbf{X}}{\varepsilon_r}(2 \cdot r - d)^2 & d \leq 2.5 \cdot r, \end{cases} \tag{5}$$

where $\delta\mathbf{X}$ is the distance vector from the centerline markers of two nearby filaments, d is the distance between the centerline markers, r is the radius of the aerodynamic cylindrical shell and $\varepsilon_r = 5e-5$ is a small positive stiffness parameter for particle-particle collisions. For the interactions between the filaments and the wall, the distance between the centerline markers is replaced by the distance between a marker and the imaginary marker with respect to the wall.

The equations governing the fluid flow are advanced in time using a semi-implicit projection method, where all terms treated explicitly are advanced using a 3^{rd} order Runge-Kutta scheme, and all terms treated implicitly are advanced using a 2^{nd} order Crank-Nicholson scheme. All spatial derivatives are discretized using second-order central-differences on a staggered grid. A weak coupling schemes was utilized to couple the two sets of equations. The code is parallelized using a domain decomposition approach in the streamwise direction.

PROBLEM SETUP

A turbulent channel flow case is considered where the filaments are located on the bottom wall. Fig. 3 shows the setup of the simulation along with the filaments in their underformed state. The computational domain extends $2.8h \times 2h \times 1.4h$ in the streamwise, wall normal and spanwise directions respectively, where h denotes the half-channel height. The pressure gradient was adjusted to maintain a constant bulk velocity U_b. The grid utilizes $400 \times 200 \times 282$ points in x, y and z respectively. The Reynolds number based on the half channel height and the bulk velocity set to $Re_b = 4000$. No-slip boundary conditions were imposed on the bottom and top walls while periodic boundary conditions were used in the streamwise and spanwise directions. When a portion of a filament crossed over one end of the domain in either x or z direction it was copied in a periodical fashion at the other end. A simulation without the filaments was run to ensure that the computational domain and grid resolution were sufficient to capture the flow physics. The Reynolds number based on the wall friction velocity u_τ is $Re_\tau = 242$. The grid resolution in wall units was $\Delta y^+ = 0.2$ for the first point at the wall and $\Delta x^+ = \Delta z^+ = 1.7$. Fig. 4 compares the velocity profile and Reynolds stresses to the reference DNS results by Moser *et al.* (1999). The agreement is very good.

Three cases with different filament bending rigidity, γ, were investigated. The filaments were arranged as a series of rows on the bottom wall. Each successive row was staggered with respect to the other ones. There are a total of six rows and five filaments per row giving a total of 30 filaments on the bottom wall. In their undeformed state the filaments have the following shape:

$$x = L \cdot cos(0.72\pi s), y = L \cdot sin(0.72\pi s) \tag{6}$$

where L is the filament length, s is the arclength parameter going from 0 at the bottom to 1 at the free end. The resulting shape is shown in Fig. 3. The length L and diameter d_f of the filaments are all h and $0.07h$ respectively resulting in an aspect ratio of 14. In the undeformed state the penetration length k defined as the ratio of the maximum filament height to the channel half height is 0.45. Near the maximum height the canopy has an open area ratio of approximately 80%. The grid resolution is such that there are approximately 15 points across the filament diameter.

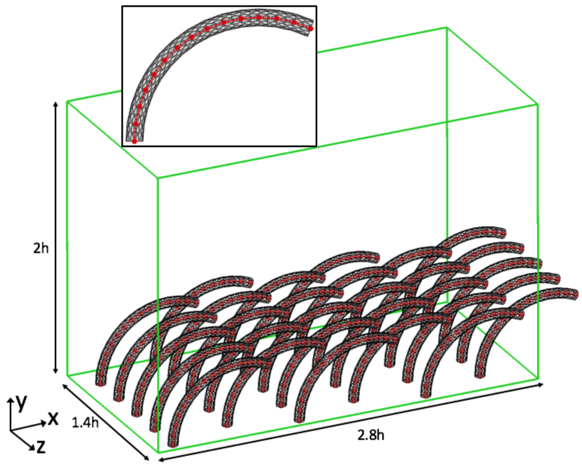

Figure 3. Computational domain of turbulent channel with filaments at the bottom wall. The subset shows a schematic illustration of the Langrangian markers at the core of the filaments used for the kinematics and the triangular mesh used in the fluid structure interaction.

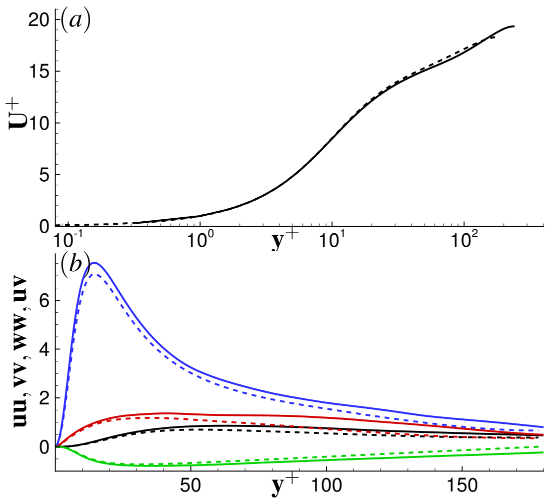

Figure 4. a) Velocity profiles and b) Reynolds stresses in a turbulent channel without filaments. Solid lines represent DNS at $Re_\tau = 240$ and dashed lines are from Moser *et al.* (1999) at $Re_\tau = 180$.

The three cases are summarized in Table 1. The ratio of fluid to solid density was $\alpha = 0.5$ and the Froude number $Fr = 1.0e-6$ for all cases. For case A the filaments are rigid and do not move. In contrast, case C is characterized by highly flexible filaments, while case B is an intermediate case. The simulations were initialized with the solution from the turbulent smooth wall channel and were integrated until the pressure gradient reached a quasi-steady value. Statistics were collected over a period of at least $100h/U_b$. Conditional averaging was employed to sample points that are only on the fluid side.

RESULTS

Fig. 5 shows the average position of the filament, which is an ensemble average of the time average position of all the filaments. In general the filaments are pushed in the direction of the flow and their height is reduced. For

Table 1. Summary of cases.

Case	Re	α	γ	k_0	k
A	4000	0.5	rigid	0.50	0.50
B	4000	0.5	3e-5	0.50	0.48
C	4000	0.5	1e-5	0.50	0.29

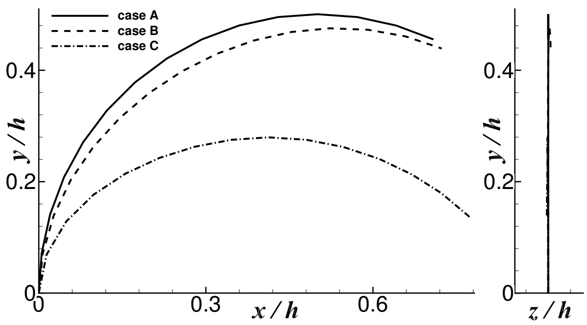

Figure 5. Time and ensemble average of the filament position for the three cases. a) View from a x-y plane and b) view from a y-z plane.

case B the maximum height is only slightly reduced to 0.48 while for case C the maximum height is reduced by almost half. Fig. 6a shows the average velocity profiles for the three cases. Despite the large open area ratio there is a shift of the centerline velocity towards the top wall for all cases. At the bottom wall there is a significant momentum deficit caused by the presence of the filaments. As the bending rigidity γ decreases and the filaments are pushed closer to the wall the momentum deficit increases. The profiles of the turbulent kinetic energy, k, are shown in Fig. 6b. At the top wall (no filaments) the peak in k occurs very close to the wall. At the bottom wall the levels of k at the corresponding distance from the wall are considerably lower. This is true for all cases and it suggests that the turbulence structure typically found in wall bounded flows, such as high and low speed streaks, is significantly altered by the filaments. The peak shifts away from the wall at a location just above the canopy. As the filaments become more flexible the magnitude of the peak is reduced. The profiles of the Reynolds stresses $\overline{u'v'}$ shown in Fig. 6c behave in a similar way.

To better illuminate the behavior the statistics a look into the instantaneous flow dynamics is presented. Fig. 7a shows contours of the instantaneous spanwise vorticity, ω_z, on a vertical plane cutting through the middle of the channel for case B. The vorticity levels between the bottom wall and the canopy formed by the flexible filaments are weaker suggesting that there are less organized structures in that region. Most of the structures are located near the edge of the canopy. These structures interact with the filaments generating vorticity around the filaments that is shed off into the flow. Fig. 7b shows contours of the streamwise fluctuation u' at a plane parallel to the wall. The location of the plane is at $y = 0.55h$ corresponding to the peak in k shown in Fig. 6b. The filaments generally move in the vertical direction and their streamwise velocity is small. As a result they slow down the flow and create wakes behind them. In areas where there are no filaments or between filaments the flow velocity is much higher. This difference in the velocity

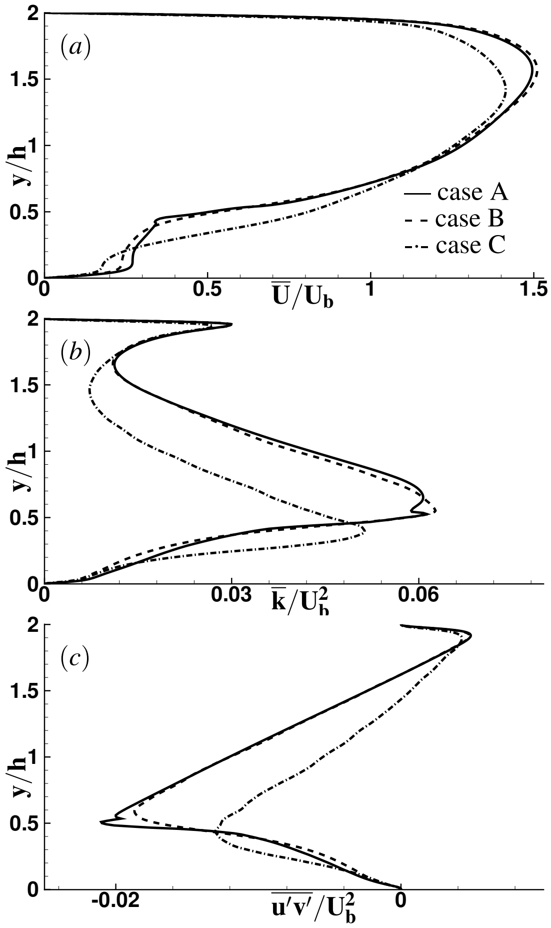

Figure 6. a) Velocity profiles and b) turbulent kinetic energy k and c) Reynolds stresses for turbulent channel with filaments.

is of the order of magnitude of the bulk velocity U_b which contribute to the relative large peak in k.

A similar behavior is observed for the case of the more flexible filaments shown in Fig. 8. The filaments are more randomly deflected and do not retain their predeformed shape. Since they are much closer to the wall the local velocity is smaller and as a result the wakes are weaker and also the velocity fluctuations are smaller.

SUMMARY

The present work explores the structure of turbulent flow over elastic micro-structures laid on an impermeable wall. The filamentous layer consists of an array of slender flush mounted flexible cylinders. The dynamic deformations of the cylinders are governed by an inextensible Kirchhoff rod model, which is well suited to model such structures: it enables control of the undeformed shape and flexibility, among other parameters to match the characteristics of the bio-inspired canopies considered in the present study. We considered a turbulent channel flow case, where the bottom wall was covered by filaments with different flexibility. Three cases were considered: rigid filaments, highly flexible filaments, and one in between. Overall, at the bottom wall a significant momentum deficit, caused by the presence of the filaments, is observed. As the bending rigidity decreases and the filaments are pushed closer to the wall, the momentum deficit increases. As a result the turbu-

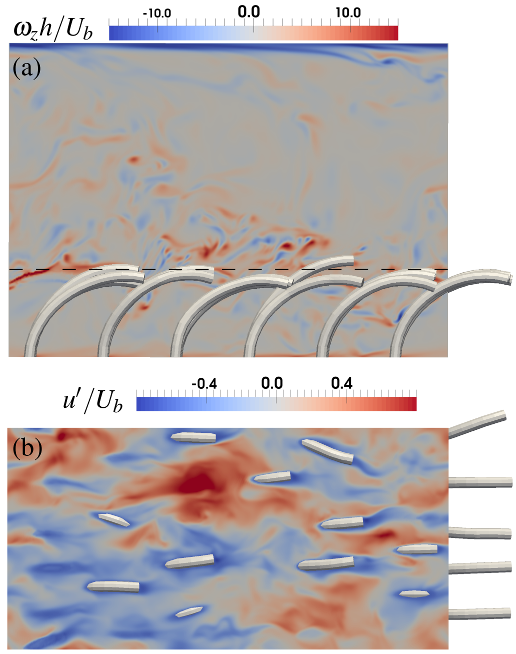

Figure 7. a) Contours of instantaneous spanwise vorticity ω_z on a spanwise plane cutting through the middle of the channel, b) contours of streamwise velocity fluctuations u' on a horizontal plane at $y = 0.55h$ for case B. The location of the horizontal plane is shown with a dashed line in the top figure.

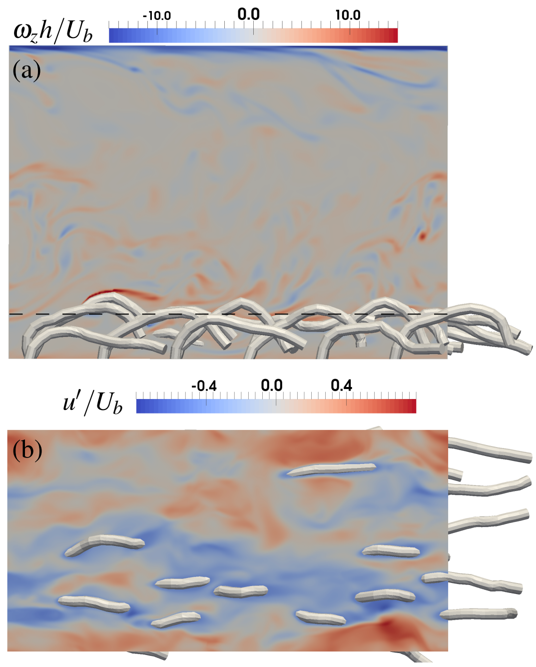

Figure 8. a) Contours of instantaneous spanwise vorticity ω_z on a spanwise plane cutting through the middle of the channel, b) contours of streamwise velocity fluctuations u' on a horizontal plane at $y = 0.30h$ for case C. The location of the horizontal plane is shown with a dashed line in the top figure.

lent kinetic energy pick is amplified and moves close the top of the average location of the filament tips. DNS exploring a wider parametric range are ongoing.

REFERENCES

Balaras, Elias 2004 Modeling complex boundaries using an external force field on fixed cartesian grids in large-eddy simulations. *Computers & Fluids* **33** (3), 375–404.

Brucker, Ch. 2011 Interaction of flexible surface hairs with near-wall turbulence. *Journal of Physics: Condensed Matter* **23** (18), 184120.

Clark, Ian, Devenport, William, Jaworski, Justin, Daly, Conor, Peake, Nigel & A. Glegg, Stewart 2014 The noise generating and suppressing characteristics of bio-inspired rough surfaces. In *20th AIAA/CEAS Aeroacoustics Conference*.

Geyer, Thomas, Sarradj, Ennes & Fritzsche, Christoph 2013 Silent owl flight: Comparative acoustic wind tunnel measurements on prepared wings. *Acta Acustica united with Acustica* **99**, 139–153.

Huang, Wei-Xi, Shin, Soo Jai & Sung, Hyung Jin 2007 Simulation of flexible filaments in a uniform flow by the immersed boundary method. *Journal of Computational Physics* **226** (2), 2206 – 2228.

Klan, S., Burgmann, S., Bachmann, T., Klaas, M., Wagner, H. & Schrder, W. 2012 Surface structure and dimensional effects on the aerodynamics of an owl-based wing model. *European Journal of Mechanics - B/Fluids* **33**, 58 – 73.

Kuwata, Y. & Suga, K. 2017 Direct numerical simulation of turbulence over anisotropic porous media. *Journal of Fluid Mechanics* **831**, 4171.

Le Bars, M. & Worster, M. Grae 2006 Interfacial conditions between a pure fluid and a porous medium: implications for binary alloy solidification. *Journal of Fluid Mechanics* **550**, 149173.

Mehta, Rabindra D. & Pallis, Jani Macari 2004 *Tennis Ball Aerodynamics and Dynamics*, pp. 99–124. Boston, MA: Springer US.

Mei, C.C. & Vernescu, B. 2010 *Homogenization methods for multiscale mechanics*. World Scientific.

Moser, R. D., Kim, J. & Mansour, N. N. 1999 Direct numerical simulation of turbulent channel flow up to Re=590. *Physics of Fluids* **11**, 943–945.

Pinelli, Alfredo, Omidyeganeh, Mohammad, Brücker, Christoph, Revell, Alistair, Sarkar, Abhishek & Alinovi, Edoardo 2017 The pelskin project: part iv—control of bluff body wakes using hairy filaments. *Meccanica* **52** (7), 1503–1514.

Sundin, Johan & Bagheri, Shervin 2019 Interaction between hairy surfaces and turbulence for different surface time scales. *Journal of Fluid Mechanics* **861**, 556584.

Tian, Fang-Bao, Luo, Haoxiang, Zhu, Luoding, Liao, James C. & Lu, Xi-Yun 2011 An efficient immersed boundary-lattice boltzmann method for the hydrodynamic interaction of elastic filaments. *Journal of Computational Physics* **230** (19), 7266 – 7283.

Wan, Decheng & Turek, Stefan 2007 An efficient multigrid-fem method for the simulation of solidliquid two phase flows. *Journal of Computational and Applied Mathematics* **203** (2), 561 – 580, special Issue: The first Indo-German Conference on PDE, Scientific Computing and Optimization in Applications.

Whitaker, S. 1993 *The method of volume averaging*. Springer.

Winzen, Andrea, Klaas, Michael & Schröder, Wolfgang 2013 High-speed piv measurements of the near-wall flow field over hairy surfaces. *Experiments in Fluids* **54** (3), 1472.

Yang, Jianming & Balaras, Elias 2006 An embedded-boundary formulation for large-eddy simulation of turbulent flows interacting with moving boundaries. *Journal of Computational Physics* **215** (1), 12–40.

‘